



Cite this: *Sustainable Energy Fuels*,  
2024, 8, 1448

# Enhanced photoelectrochemical hydrogen production *via* linked BiVO<sub>4</sub> nanoparticles on anodic WO<sub>3</sub> nanocoral structures†

Eunoak Park,  JeongEun Yoo\* and Kiyoung Lee 

Morphological properties of photoanodes are crucial for improving their photoelectrochemical (PEC) performance. In this study, we fabricated bismuth vanadate (BiVO<sub>4</sub>) nanoparticles (NPs) with an optimal size of ~10 nm, as well as nanowires composed of NPs on anodized tungsten trioxide (WO<sub>3</sub>) nanocoral structures. The linked BiVO<sub>4</sub> NPs were decorated by spin-coating, with the amount of the BiVO<sub>4</sub> precursor being controlled. Subsequently, the concentrations of Bi and V in the BiVO<sub>4</sub> precursor were determined. An optimized concentration of 0.3 M Bi and V for the linked BiVO<sub>4</sub> NPs/WO<sub>3</sub> nanocoral heterostructure led to enhanced photocurrent density and hydrogen gas-production compared to those of the pristine WO<sub>3</sub> nanocorals, yielding results that were 2.4 times higher. In particular, the incident photon-to-current conversion efficiency value at 410 nm improved by 8.3 times, as the linked BiVO<sub>4</sub> NPs attained efficient absorbance of visible light and a sufficient electron transfer pathway.

Received 29th November 2023  
Accepted 24th February 2024

DOI: 10.1039/d3se01545a

rsc.li/sustainable-energy

## 1. Introduction

Numerous efforts to produce hydrogen energy have been made using renewable energy from solar fuels to address the global energy crisis.<sup>1–3</sup> In particular, photoelectrochemical water splitting (PEC-WS) has emerged as a promising green engineering approach for generating hydrogen through direct utilization of sunlight.<sup>4,5</sup> For PEC-WS, metal oxide semiconductors are mostly used as photoelectrodes because of their beneficial bandgap and band positions for photoreactions.<sup>6</sup> However, metal oxide semiconductor photoanodes face several critical issues, such as reduced solar-to-hydrogen efficiency of PEC-WS, slow surface water oxidation, poor visible light absorption, and fast electron–hole recombination.<sup>7,8</sup>

Bismuth vanadate (BiVO<sub>4</sub>), the most promising metal oxide photoanode material for PEC-WS, has been investigated owing to its intrinsic properties such as abundance, nontoxicity, and low cost.<sup>9–11</sup> BiVO<sub>4</sub> also satisfies the requirements for an efficient photoanode by providing a narrow bandgap of 2.4 eV with a relatively negative conduction band edge of ~0 V *vs.* the reversible hydrogen electrode (RHE), and having a high optical absorption coefficient (~10<sup>4</sup>–10<sup>5</sup> cm<sup>−1</sup> at *hν* = 2.5–3.5 eV).<sup>12–14</sup> Despite these advantages, BiVO<sub>4</sub> still suffers from fast recombination of photogenerated electrons and holes because of its

low carrier mobility (~4.4 × 10<sup>−2</sup> cm<sup>2</sup> V<sup>−1</sup> s<sup>−1</sup>) and short hole diffusion length (~70 nm).<sup>15,16</sup>

To overcome these drawbacks and enhance the photo efficiency of PEC-WS, BiVO<sub>4</sub> often adopts a type-II heterojunction configuration with two or more n-type semiconductors. At the heterojunction interface between two semiconductors, a wide bandgap material offers a more negative conduction band (CB) edge, allowing electrons to move from the narrow bandgap material to the wide bandgap material.<sup>17</sup> In this context, tungsten trioxide (WO<sub>3</sub>) (~2.8 eV) has been considered the most suitable matching material for forming a type II heterojunction with BiVO<sub>4</sub>. This is because WO<sub>3</sub> has a superior electron mobility (~12 cm<sup>2</sup> V<sup>−1</sup> s<sup>−1</sup>), relatively long hole diffusion length (~150 nm), and lower CB edge of +0.41 V *vs.* RHE compared to BiVO<sub>4</sub>.<sup>18–20</sup> To fabricate WO<sub>3</sub> for the configuration of the BiVO<sub>4</sub>/WO<sub>3</sub> heterostructure, several simple approaches have been reported such as a hydrothermal method,<sup>17,21</sup> dip-coating,<sup>22</sup> spin-coating,<sup>23</sup> and anodization.<sup>24</sup> Among the various methods, the anodization method is an advantageous because W metal as a substrate can provide direct back contact under the WO<sub>3</sub> layer and can form various nanostructures with a high specific surface area by adjusting the anodization conditions (*e.g.*, electrolyte, temperature, applied potential, *etc.*). There is only one reported research study that used anodic WO<sub>3</sub> for fabricating a BiVO<sub>4</sub>/WO<sub>3</sub> heterostructure. However, the BiVO<sub>4</sub>/WO<sub>3</sub> heterostructure of anodized WO<sub>3</sub> structures and spin-coated BiVO<sub>4</sub> layers has not fulfilled the role of a photoanode for PEC-WS, because the thick BiVO<sub>4</sub> layer (~850 nm) interrupts the mobility of photogenerated electrons from BiVO<sub>4</sub> to WO<sub>3</sub>.<sup>25</sup> Thus, it is obvious that rapid electron movement is allowed only when BiVO<sub>4</sub> is as thin as a nanolayer or a nanoparticle (NP).<sup>10</sup> In

Department of Chemistry and Chemical Engineering, Inha University, 100 Inha-ro, Michuhol-gu, 22212 Incheon, South Korea. E-mail: kiyoung@inha.ac.kr; JeongEunYoo@inha.ac.kr

† Electronic supplementary information (ESI) available: FE-SEM, droplet schematics, bandgap, H<sub>2</sub> production rate, and EDX data. See DOI: <https://doi.org/10.1039/d3se01545a>



particular, metal oxide NPs have attracted attention in photoelectrochemical reactions as they provide a large reaction area, leading to improved photoreaction efficiency.

In this study, we have investigated how to fabricate BiVO<sub>4</sub> NPs on anodic WO<sub>3</sub>. In addition, we developed BiVO<sub>4</sub> NPs linked as nanowires to a WO<sub>3</sub> nanocoral structure. This is the first study on the heterojunction of BiVO<sub>4</sub> NPs and anodic WO<sub>3</sub> nanocorals. The WO<sub>3</sub> nanocoral structures on W metal were fabricated by the anodization method, as previously reported.<sup>22</sup> The linked BiVO<sub>4</sub> NPs were formed on the WO<sub>3</sub> nanocorals by the spin-coating method where, instead of deionized water, we employed an ethylene glycol-based solvent as a BiVO<sub>4</sub> precursor for the spin-coating process, since the utilization of the ethylene glycol-based BiVO<sub>4</sub> precursor allows BiVO<sub>4</sub> nanoparticles to form with sizes below 100 nm as supporting particle agglomeration on WO<sub>3</sub> layers during spin-coating. The use of ethylene glycol as the solvent for the BiVO<sub>4</sub> precursor has not been previously reported. Furthermore, we focus on the amount of the BiVO<sub>4</sub> precursor used during spin-coating to construct linked BiVO<sub>4</sub> NPs on WO<sub>3</sub> nanocorals and determine their morphologies, crystal structures, and PEC performances with different precursor amounts. We then optimized the concentration of vanadium (V) in the BiVO<sub>4</sub> precursor and investigated the morphologies, compositional properties, and PEC performance of the heterostructure of the BiVO<sub>4</sub> NPs/WO<sub>3</sub> nanocorals.

## 2. Experimental

### 2.1 Materials

The following materials were used as received: ammonium fluoride (NH<sub>4</sub>F, ≥ 98%, Sigma Aldrich), sodium sulfate (Na<sub>2</sub>SO<sub>4</sub>, ≥ 99.9%, Sigma Aldrich), bismuth(III) nitrate pentahydrate (Bi(NO<sub>3</sub>)<sub>3</sub>·5H<sub>2</sub>O, ≥ 98%, Sigma Aldrich), nitric acid (HNO<sub>3</sub>, 60%, Samchun Chemicals), ethylene glycol (HOCH<sub>2</sub>CH<sub>2</sub>OH, 99.5%, Samchun Chemicals), and ammonium metavanadate (NH<sub>4</sub>VO<sub>3</sub>, 99%, Daejung Chemicals & Metals).

### 2.2 Preparation of the BiVO<sub>4</sub>/WO<sub>3</sub> photoanodes

Tungsten (W) metal (thickness: 0.1 mm, 99.95% purity, Alfa Aesar) was cut into 1.5 × 1.5 cm<sup>2</sup> and mechanically ground using a 1200 grit soft sandpaper. Next, the W metal was cleaned successively with acetone, ethanol, and deionized (DI) water using an ultrasonicator, and then dried with nitrogen (N<sub>2</sub>) gas. W metal was anodized in a 1 M Na<sub>2</sub>SO<sub>4</sub> solution containing 0.5 wt% NH<sub>4</sub>F at 15 °C. The thickness of WO<sub>3</sub> nanocorals was increased with increase in anodization time from 1 h to 5 h, to approximately 460, 540, 610, 660 and 690 nm, respectively. Among them, WO<sub>3</sub> anodized for 3 h was used as the substrate. During anodization, a constant voltage of 40 V was applied to W using a DC power source (ODA-EX300-4), and current density *versus* time curves were recorded using a Keithley 2000. After anodization, the anodic WO<sub>3</sub> nanocorals were rinsed with DI water and dried with N<sub>2</sub> gas. Heat-treatment was performed in a tubular furnace at 500 °C under an argon (Ar) atmosphere for 2 h to crystallize the anodized WO<sub>3</sub> nanocoral film. Then, the BiVO<sub>4</sub> NPs were decorated onto the WO<sub>3</sub> nanocoral films by spin-coating. The BiVO<sub>4</sub>

precursor solution for spin-coating was prepared by dissolving 0.15 (0.3), 0.23 (0.44), 0.3 (0.59), and 0.6 M (1.18) NH<sub>4</sub>VO<sub>3</sub> in a mixture of 10 mL HNO<sub>3</sub> and 20 mL ethylene glycol. After complete dissolution, 0.3 M (2.25) Bi(NO<sub>3</sub>)<sub>3</sub>·5H<sub>2</sub>O was added and then the solution was stirred for 30 min. After dropping 5, 10, and 30 μL of the precursor onto the WO<sub>3</sub> substrate, the samples were rested for 1 min so that the precursor penetrates to the bottom of the nanocoral structures. The spin-coating process was performed at 500 rpm for 60 s, 1000 rpm for 30 s, and 3000 rpm for 3 s for the precursor mixture solution and was repeated 3 times. Between each cycle, the BiVO<sub>4</sub>/WO<sub>3</sub> samples were heat-treated in a box furnace at 100 °C for 5 min. After the spin-coating process, the samples were annealed at 550 °C under an air atmosphere using the box furnace for 1 h.

### 2.3 Characterization

The morphologies of the WO<sub>3</sub> and BiVO<sub>4</sub>/WO<sub>3</sub> photoanodes were observed using a field-emission scanning electron microscope (FE-SEM, S-4300, Hitachi). To characterize the crystalline structures of the photoanodes, X-ray diffraction (XRD, X'Pert PRO MRD, Phillips) with a Cu-Kα radiation source and field emission transmission electron microscopy (FE-TEM, JEM-2100F, JEOL) were used. Raman scattering measurements (LabRAM HR Evolution, HORIBA) were obtained using 532 nm lasers. The analysis was conducted at the Inha University Core Facility Center for Sustainable Energy.

### 2.4 Photoelectrochemical measurements

0.5 M Na<sub>2</sub>SO<sub>4</sub> solution, silver/silver chloride (Ag/AgCl, 3 M KCl), a Pt mesh, and BiVO<sub>4</sub>/WO<sub>3</sub> photoanodes were used as the electrolyte, and reference, counter, and working electrodes, respectively. Photocurrent density, electrochemical impedance spectroscopy (EIS), and hydrogen (H<sub>2</sub>) gas production were measured using a potentiostat (VSP, Bio-Logics) and a solar simulator (LCS-100, Oriel Instruments) with a 100 W xenon (Xe) arc lamp (100 mW cm<sup>-2</sup>). To record the photocurrent density, linear sweep voltammetry (LSV) was performed at a scan rate of 5 mV s<sup>-1</sup>. The obtained potential was converted into a RHE potential using the following equation:

$$E_{\text{RHE}} = E_{\text{Ag/AgCl}} + (0.0591 \times \text{pH}) + E_{\text{Ag/AgCl}}^{\circ}$$

and

$$E_{\text{Ag/AgCl}} (3 \text{ M KCl}) = 0.1976 \text{ V at } 25 \text{ }^{\circ}\text{C}$$

EIS was performed in the range of 30 kHz–10 MHz at 1.23 V *vs.* RHE. To evaluate PEC H<sub>2</sub>-gas production at 1.23 V *vs.* RHE, 200 μL gas was taken from the sealed quartz tube reactor every half hour and injected into a gas chromatograph with a TCD detector (GC/MSD 5975C, Agilent Technologies). The incident photon-to-current conversion efficiency (IPCE) was measured at 1.23 V *vs.* RHE using a monochromator (MonoRa200, DONG-WOO OPTRON) and various bandpass filters with a Xe lamp (300 W, OMA). The IPCE was calculated using the following equation:



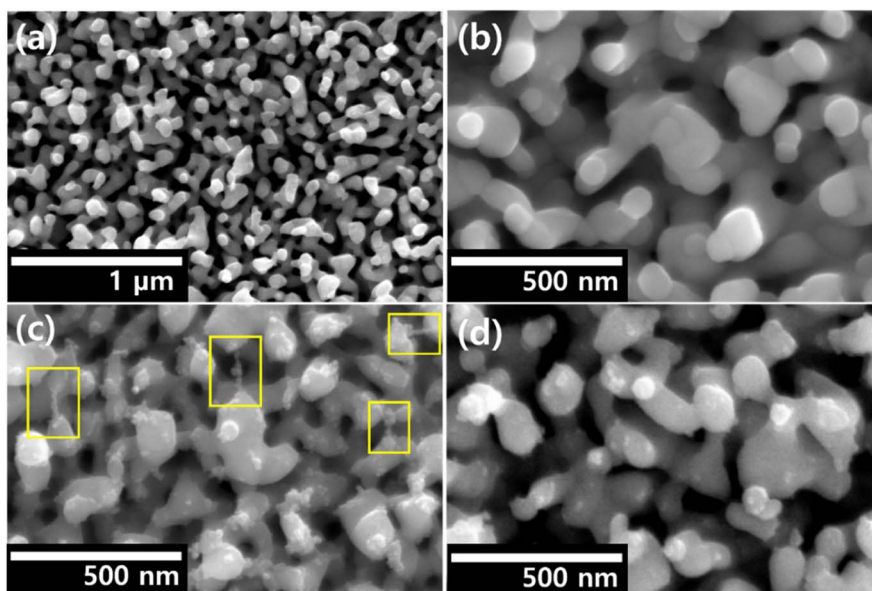


Fig. 1 FE-SEM image of (a)  $\text{WO}_3$  nanocorals, (b) 5-BW, (c) 10-BW, and (d) 30-BW.

$$\text{IPCE}(\%) = \frac{hc \times J_{\text{ph}}}{\lambda \times P} \times 100,$$

where  $h$  is Planck constant,  $c$  is the velocity of light,  $J_{\text{ph}}$  is the photocurrent density,  $\lambda$  is the incident wavelength, and  $P$  is power density of each wavelength.

### 3. Results and discussion

#### 3.1 Formation of linked $\text{BiVO}_4$ NPs on $\text{WO}_3$ nanocorals

Fig. 1a shows the morphology of  $\text{WO}_3$  nanocoral anodized W metal described in our previous report.<sup>24</sup> The  $\text{WO}_3$  nanocorals have thick branches and round edges with a high surface area, which can support the formation of NPs, and the length of the nanocoral structures is  $\sim 550$ – $600$  nm (Fig. S1†). All the  $\text{BiVO}_4/\text{WO}_3$  (BW) heterostructures formed by the anodization and spin-coating processes contained  $\text{BiVO}_4$  NPs on the  $\text{WO}_3$  nanocorals as presented in Fig. 1b–d. During the spin-coating process, the precursor amounts were controlled to be 5, 10, and 30  $\mu\text{L}$ , and the heterostructural  $\text{BiVO}_4$  NPs/ $\text{WO}_3$  nanocorals

fabricated with these precursor amounts were labelled as 5-BW, 10-BW, and 30-BW, respectively. Following heat treatment in air, a 5–10 nm size of the well-spread  $\text{BiVO}_4$  NPs was observed on the  $\text{WO}_3$  nanocorals. The formation of  $\text{BiVO}_4$  NPs on the nanocorals was related to the hydrophilicity of the anodic  $\text{WO}_3$  nanocorals. After anodization, normally the metal oxide has hydrophilicity.<sup>26</sup> The anodic metal oxide is hydrophilic, but the rest of the metal surface is relatively hydrophobic; thus, the precursor prefers to remain on the anodized surface, where it forms a droplet, as shown in Fig. S2.† As the 5  $\mu\text{L}$  precursor amount is a small quantity, it was not sufficient to form numerous  $\text{BiVO}_4$  NPs compared to a 10  $\mu\text{L}$  amount, and thus the NPs were rarely located as shown in Fig. 1b. However, a 10  $\mu\text{L}$  precursor droplet can withstand speeds up to 3000 rpm, allowing for a larger quantity of the precursor to remain on the  $\text{WO}_3$  nanocoral surface, resulting in a large amount of  $\text{BiVO}_4$  NPs being coated on the  $\text{WO}_3$  nanocorals for 10-BW. In particular, the NPs are linked as nanowires from one  $\text{WO}_3$  nanocoral branch to another, as shown in Fig. 1c. We expected 30-BW to contain more NPs than 10-BW; however, 30-BW displayed only

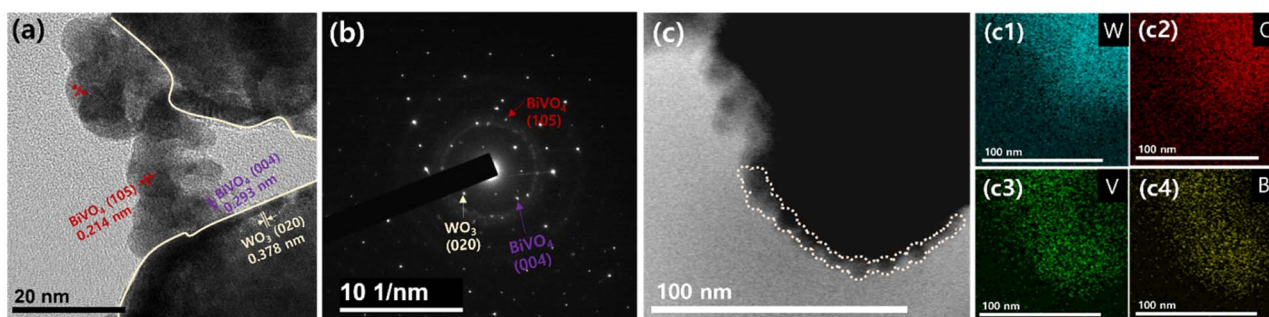


Fig. 2 (a) FE-TEM image of 10-BW, (b) corresponding SAED pattern of (a), (c) TEM image obtained in the HADDF mode of 10-BW, and (c1–c4) corresponding elemental analysis by EDS mapping of W, O, V, and Bi.





Fig. 3 XRD patterns of  $\text{WO}_3$  nanocrystals and  $\text{BiVO}_4/\text{WO}_3$  heterostructures of 5-BW, 10-BW, and 30-BW.

well-perched NPs on the  $\text{WO}_3$  nanocrystals without linking (Fig. 1d). This is because 30  $\mu\text{L}$  of the precursor is comparatively easy to disperse to the outer area than 10  $\mu\text{L}$  of the precursor when the centrifugal force interacts with the droplet during spin-coating (Fig. S2†). In the case where some part of the droplet dispersed to the non-anodized metal surface and the droplet suddenly flattened, the droplet flowed off the substrate, reducing the precursor amount.

The TEM image of 10-BW in Fig. 2a showed  $\sim 10$  nm  $\text{BiVO}_4$  NPs with lattice spacings of 0.214 and 0.293 nm representing the planes of (1 0 5) and (0 0 4), respectively, and the  $\text{WO}_3$  nanocrystals with a lattice spacing of 0.378 nm, corresponding to the (0 2 0) plane. The selected-area electron diffraction (SAED) pattern (Fig. 2b) confirms a polycrystalline structure; the (0 2 0) plane corresponds to monoclinic  $\text{WO}_3$  and the (1 0 5) and (0 0 4) planes correspond to monoclinic  $\text{BiVO}_4$ . High-angle annular dark-field (HAADF)-scanning TEM reveals well configured  $\text{BiVO}_4$  NPs and  $\text{WO}_3$  (Fig. 2c). The NPs were linked to the surface of  $\text{WO}_3$ , and energy-dispersive X-ray spectroscopy (EDS) elemental mapping revealed that the  $\text{BiVO}_4$  NPs were uniformly distributed on the  $\text{WO}_3$  surface.

The crystalline phases of the  $\text{WO}_3$  nanocrystals (5-BW, 10-BW, and 30-BW) were examined using XRD, as illustrated in Fig. 3. Peaks corresponding to W metal were observed at  $40.2^\circ$ ,  $58.2^\circ$ , and  $73.2^\circ$  for the  $\text{WO}_3$  nanocrystals, whereas only the  $40.2^\circ$  peak was observed for the BW samples. The XRD patterns of the  $\text{WO}_3$  nanocrystal layer show peaks at  $23.0^\circ$ ,  $23.5^\circ$ ,  $24.2^\circ$ ,  $26.5^\circ$ ,  $33.1^\circ$ ,  $34.0^\circ$ ,  $41.6^\circ$ ,  $49.9^\circ$ , and  $55.7^\circ$  indexed to the (0 0 2), (0 2 0), (2 0 0), (1 2 0), (0 2 2), (2 2 0), (2 2 2), (2 3 2), and (4 0 2) planes, respectively. The  $\text{WO}_3$  nanocrystals exhibited well-crystallized monoclinic  $\text{WO}_3$  phases (JCPDS #089-4476).<sup>27,28</sup> The XRD patterns of all the BW samples exhibited peaks at  $18.9^\circ$ ,  $28.9^\circ$ ,  $30.5^\circ$ ,  $40.2^\circ$ ,  $60.0^\circ$ , and  $76.5^\circ$  corresponding to the (0 1 1), (1 1 2), (0 0 4), (0 2 0), (1 2 1), (2 2 4), and  $(-1\ 3\ 6)$  planes, respectively, which are the monoclinic phases of  $\text{BiVO}_4$  (JCPDS #075-1866).<sup>29,30</sup> Although 5-BW showed lower  $\text{BiVO}_4$  peak intensities

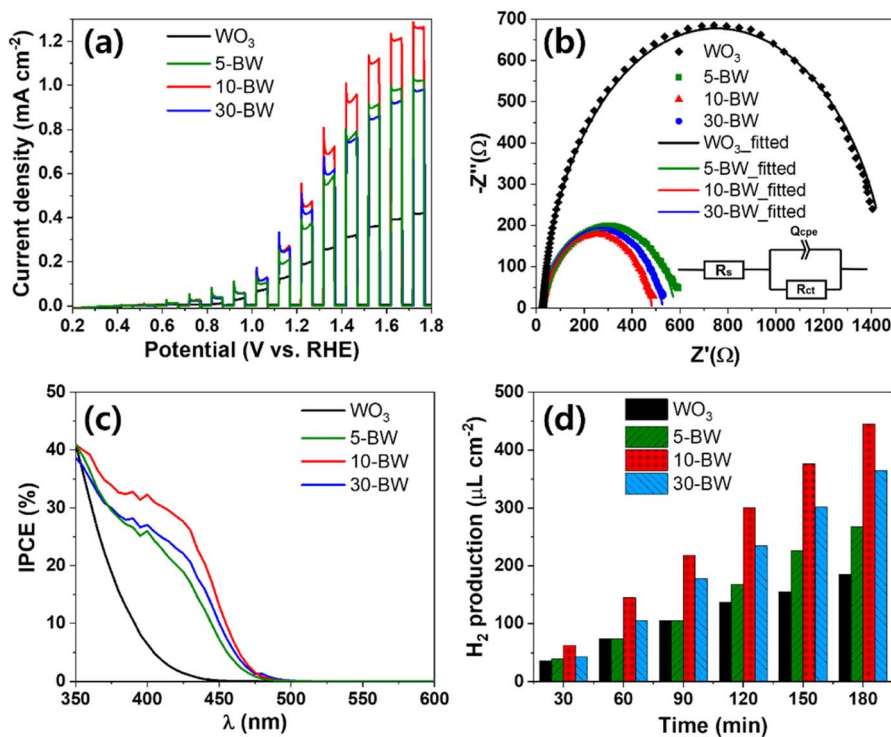


Fig. 4 Photoelectrochemical performances of the  $\text{WO}_3$  nanocrystals and  $\text{BiVO}_4/\text{WO}_3$  photoanodes of 5-BW, 10-BW, and 30-BW: (a) photocurrent densities by linear sweep voltammetry, (b) Nyquist plots and equivalent circuits, (c) PEC  $\text{H}_2$  production diagram as a function of time, and (d) IPCE spectra.





Fig. 5 Schematic illustration of 10-BW and its mechanism of charge transfer and the antenna effect.

at  $18.9^\circ$  and  $30.5^\circ$  owing to the quantity of  $\text{BiVO}_4$ , the 10-BW and 30-BW peak intensities were similar. This indicates that  $10 \mu\text{L}$  of the  $\text{BiVO}_4$  precursor is sufficient to form well-crystallized  $\text{BiVO}_4$  NPs that are to be used as photoanodes.

The chopped linear sweep voltammetry (LSV) curves with the PEC performance of 5-BW, 10-BW, and 30-BW are illustrated in Fig. 4a. Compared to the pristine  $\text{WO}_3$  nanocorals, all the BW photoanodes exhibited a higher photocurrent density, indicating that the heterostructural BW achieved an improved photocurrent density. The highest photocurrent density of  $0.45$

$\text{mA cm}^{-2}$  at  $1.23 \text{ V vs. RHE}$  was obtained with the  $10 \mu\text{L}$  spin-coated  $\text{BiVO}_4/\text{WO}_3$  photoanode, and it was 2.4 times higher than that obtained for the  $\text{WO}_3$  nanocorals ( $0.19 \text{ mA cm}^{-2}$  at  $1.23 \text{ V vs. RHE}$ ). The  $\text{BiVO}_4/\text{WO}_3$  photoanodes of 30-BW and 5-BW were followed to  $0.42$  and  $0.35 \text{ mA cm}^{-2}$  at  $1.23 \text{ V vs. RHE}$ . The 5-BW sample exhibited the lowest photocurrent density owing to the extremely small quantity of  $\text{BiVO}_4$  NPs on the  $\text{WO}_3$  layer. The fitted EIS Nyquist plots of the 5-BW, 10-BW, 30-BW, and  $\text{WO}_3$  nanocorals are depicted in Fig. 4b. In addition, the applied equivalent circuit consisting of the solution resistance

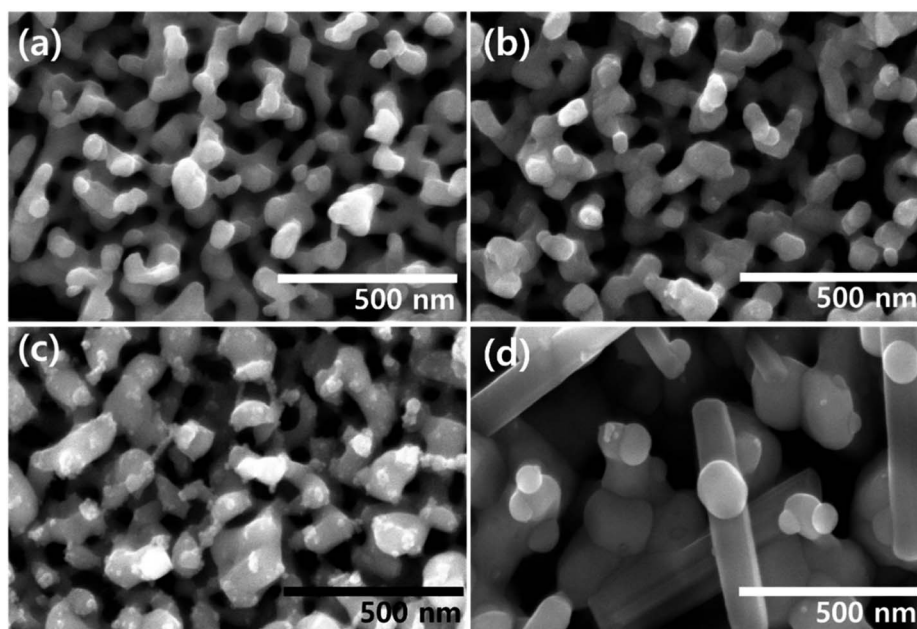


Fig. 6 FE-SEM image of  $\text{BiVO}_4/\text{WO}_3$  photoanodes depending on V concentration of the  $\text{BiVO}_4$  precursor; (a) 0.15, (b) 0.23, (c) 0.3, and (d) 0.6 M.



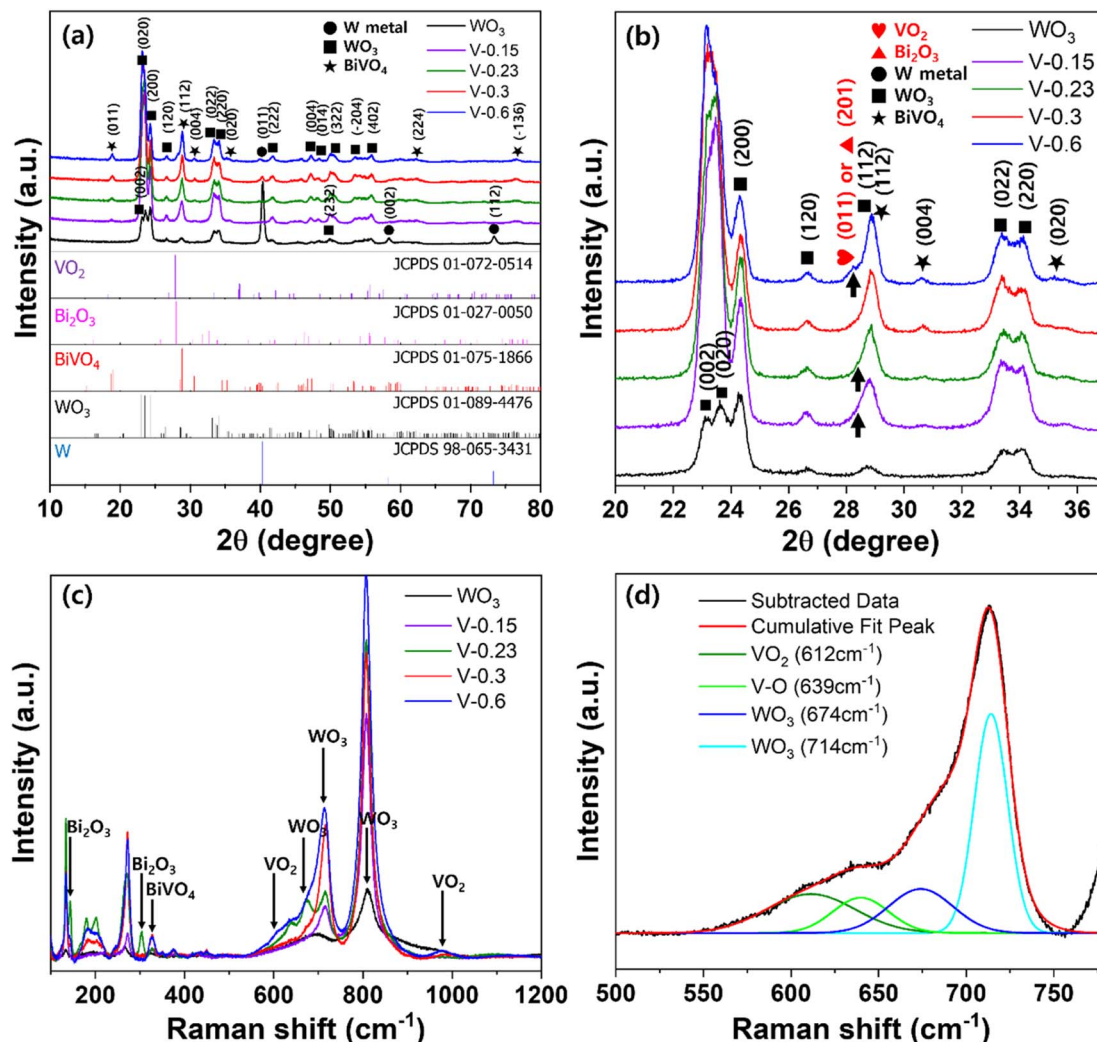
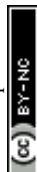


Fig. 7 (a) XRD patterns of BiVO<sub>4</sub>/WO<sub>3</sub>, (b) enlargement of (a) from 20° to 37°, (c) Raman spectra of BiVO<sub>4</sub>/WO<sub>3</sub> photoanodes depending on V concentrations of 0.15, 0.23, 0.3, and 0.6 M for the BiVO<sub>4</sub> precursor; and (d) peak separation of V-0.6 at (c) from 500 to 750 cm<sup>-1</sup>.

( $R_s$ ), charge transfer resistance ( $R_{ct}$ ), and constant phase element ( $Q_{cpe}$ ) is shown in the inset. The sequence of charge transfer resistance values was in line with the photocurrent densities: 10-BW (457.3  $\Omega$ ) < 30-BW (506.2  $\Omega$ ) < 5-BW (561.1  $\Omega$ ) < WO<sub>3</sub> nanocorals (1450  $\Omega$ ). After the PEC measurements, 10-BW showed an identical morphology and crystal structure (Fig. S3–S4<sup>†</sup>). In addition, the chemical composition of each element, except V, displayed identical intensities as illustrated in Fig. S5.<sup>†</sup> The decreased intensity of V is due to dissolution of V<sup>5+</sup> ions, and the Bi peaks slightly shifted to higher binding energies owing to the strong influence of O bonding energy on Bi after the removal of V. However, this had negligible impact on the changes in performance. As presented in Fig. 4c, the linked BiVO<sub>4</sub> NPs of 10-BW achieved the highest IPCE values of 39% at 360 nm and 30% at 410 nm. At 350 nm, the WO<sub>3</sub> nanocorals, 5-BW, and 10-BW showed an approximate value of 40%, but 10-BW exhibited superior absorbance of light, even at a longer wavelength of 350 nm. The sequence of the IPCE values of the BW samples was 5-BW (36%), 30-BW (35%), and WO<sub>3</sub>

nanocorals (31%) at 360 nm; meanwhile, at 410 nm, the order changed to 30-BW (25%), 5-BW (23%), and WO<sub>3</sub> nanocorals (4%). The two IPCE values of 5-BW and 30-BW were reversed at 372 nm, implying that 30-BW absorbed more visible light than 5-BW. Conversely, 5-BW can absorb more UV light than 30-BW. This indicates that a higher absorbance of visible light, instead of UV light, results in an improved PEC efficiency. The bandgaps evaluated using IPCE data are shown in Fig. S6.<sup>†</sup> Even though the amounts of the precursor were significantly different, the bandgaps of the WO<sub>3</sub> nanocorals, 5-BW, 10-BW, and 30-BW were relatively similar, that is, 2.80, 2.54, 2.53, and 2.55 eV, respectively. PEC H<sub>2</sub>-production under solar light irradiation for 3 h is depicted in Fig. 4d. The H<sub>2</sub> amounts of WO<sub>3</sub> nanocorals, 5-BW, 10-BW, and 30-BW were 185.6, 267.6, 445.3, and 365.5  $\mu\text{L cm}^{-2}$ , respectively, and they linearly increased with increasing reaction time. H<sub>2</sub> production is interrelated with photocurrent density, and high photocurrent density led to a high production rate; thus 10-BW obtained a higher H<sub>2</sub> production rate of 123.0  $\mu\text{L h}^{-1} \text{cm}^{-2}$  compared to



30-BW ( $86.3 \mu\text{L h}^{-1} \text{cm}^{-2}$ ) and 5-BW ( $33.6 \mu\text{L h}^{-1} \text{cm}^{-2}$ ), as shown in Fig. S7.† The faradaic efficiency for PEC  $\text{H}_2$ -production using the optimal 10-BW was calculated to be 86%. In addition, the mixed structures of  $\text{BiVO}_4$  NPs and linked chains of NPs of 10-BW significantly improved the PEC efficiency by providing a charge-transfer pathway for electrons or holes to move easily toward  $\text{WO}_3$  or  $\text{BiVO}_4$  (Fig. 5). Moreover, the linked  $\text{BiVO}_4$  NPs can transfer photon energy from one NP to another, which is called the antenna effect<sup>31</sup> resulting in high PEC activities. The linked  $\text{BiVO}_4$  NPs also connected one  $\text{WO}_3$  nanocoral to another during the migration of electron-hole pairs (excitons). Once the exciton is transferred to the  $\text{WO}_3$  nanocoral, the exciton is separated into both electron and hole, and the electron/hole transfer is activated.<sup>32</sup> Then, each transferred electron migrates to the  $\text{WO}_3$  nanocoral, and the holes are transferred to the  $\text{BiVO}_4$  NPs. Furthermore, numerous generated excitons increase solar-to-hydrogen conversion efficiency,<sup>33</sup> resulting in the generation of a high amount of  $\text{H}_2$ .

### 3.2 Optimization of the $\text{BiVO}_4$ precursor

To improve the quality of  $\text{BiVO}_4$ , V concentrations in the  $\text{BiVO}_4$  precursor were controlled to be 0.15, 0.23, 0.3, and 0.6 M, and samples with these concentrations were labelled as V-0.15, V-0.23, V-0.3, and V-0.6, respectively, while the bismuth (Bi) concentration was fixed at 0.3 M. Each precursor was spin-coated on  $\text{WO}_3$  nanocorals with 10  $\mu\text{L}$  optimized for PEC performance. Fig. 6 presents the different morphologies of the

BW samples obtained with different V concentrations in the  $\text{BiVO}_4$  precursors. In the SEM image of V-0.15 (Fig. 6a),  $\text{BiVO}_4$  NPs were not observed, and the morphology was identical to that of the pristine  $\text{WO}_3$  nanocorals.  $\text{BiVO}_4$  NPs were rarely present in the SEM images of V-0.23, as illustrated in Fig. 6b. Linked  $\text{BiVO}_4$  NPs were observed only for V-0.3, as shown in Fig. 6c. The quantity of  $\text{BiVO}_4$  NPs increased with an increase in the V concentration from 0.23 M to 0.3 M. However, when the V concentration was increased to 0.6 M, some nanorods are suddenly obtained along with  $\text{BiVO}_4$  NPs as shown in Fig. 6d. The nanorods were composed of V and oxygen (O), as shown in Fig. S8.† Vanadium oxide nanorods were formed because of the high concentration of V.

The XRD patterns of the V-controlled  $\text{BiVO}_4/\text{WO}_3$  photoanodes are shown in Fig. 7a. The monoclinic phases of  $\text{WO}_3$  and  $\text{BiVO}_4$  exhibit the same patterns as those shown in Fig. 3. However, all the samples, except V-0.3, demonstrated a broad peak with a strong shoulder peak at approximately  $28^\circ$ , particularly V-0.6 (Fig. 7b). As shown in Fig. 6d, V-0.6 has vanadium oxide nanorods at the surface; thus, the peak at  $27.89^\circ$  was predicted to be of  $\text{VO}_2$  (JCPDS #072-0514),<sup>34</sup> whereas the lack of V in the V-0.15 or V-0.23 samples could lead to the formation of bismuth oxides, which are responsible for the peak at  $27.94^\circ$  (JCPDS #027-0050).<sup>35</sup> As the other peaks of  $\text{VO}_2$  or  $\text{Bi}_2\text{O}_3$  overlapped with the  $\text{WO}_3$  or  $\text{BiVO}_4$  peaks, additional peaks were not investigated.

Raman scattering measurements were conducted to precisely characterize the V-controlled  $\text{BiVO}_4$  (Fig. 7c). The



Fig. 8 Photoelectrochemical performances of  $\text{BiVO}_4/\text{WO}_3$  photoanodes depending on V concentrations of 0.15, 0.23, 0.3, and 0.6 M of the  $\text{BiVO}_4$  precursor; (a) photocurrent densities by linear sweep voltammetry, (b) Nyquist plots, (c) IPCE spectra, and (d) bandgap evaluated by IPCE measurement.



O–W–O stretching bands at 714 and 806  $\text{cm}^{-1}$  allowed for the identification of monoclinic  $\text{WO}_3$ .<sup>36</sup> The peaks for V-0.15 were comparable to those of pristine  $\text{WO}_3$ , as the  $\text{BiVO}_4$  NPs were rarely present on the surface of the  $\text{WO}_3$  nanocorals. After the formation of  $\text{BiVO}_4$ , the remaining Bi in the  $\text{BiVO}_4$  precursor with V-0.23 formed bismuth oxide. Thus, the peak of Bi–O stretching mode of  $\text{Bi}_2\text{O}_3$  at 304  $\text{cm}^{-1}$  was only observed for V-0.23.<sup>37</sup> Similarly, the residue of V in the  $\text{BiVO}_4$  precursor with V-0.6 formed vanadium oxide,  $\text{VO}_2$ ; thus, the corresponding peaks appeared at 612 and 988  $\text{cm}^{-1}$ , as shown in Fig. 6d.<sup>38,39</sup> As a result, V-0.3 showed  $\text{BiVO}_4$  peaks at 326 and 374  $\text{cm}^{-1}$  without any by-products, which were attributed to the asymmetric and symmetric deformation of  $\text{VO}_4^{3-}$ .<sup>40</sup> Therefore, 0.3 M of Bi and V is an optimal concentration as a  $\text{BiVO}_4$  precursor for fabrication of high-quality  $\text{BiVO}_4$  NPs.

The PEC performances of different V-controlled  $\text{BiVO}_4/\text{WO}_3$  photoanodes are shown in Fig. 8a. The optimal BW photoanode with V-0.3 showed the highest photocurrent density value of 0.45  $\text{mA cm}^{-2}$  at 1.23 V vs. RHE. The V-0.6 and V-0.23 samples then followed with photocurrent densities of 0.36 and 0.27  $\text{mA cm}^{-2}$  at 1.23 V vs. RHE, and 0.15 M showed an even lower photocurrent density of 0.16  $\text{mA cm}^{-2}$  at 1.23 V vs. RHE compared to pristine  $\text{WO}_3$  nanocorals. Based on the photocurrent results, the sequence of charge transfer resistance should exhibit an opposite trend: the optimal BW photoanode of V-0.3 had the lowest resistance of 486.9  $\Omega$  followed by V-0.9 (518.1  $\Omega$ ), V-0.44 (633.0  $\Omega$ ), and V-0.3 (1110  $\Omega$ ) as shown in Fig. 8b. The equivalent circuit and its components are the same as those shown in Fig. 4b. In Fig. 8c, the optimal BW photoanode (V-0.3) also shows the highest IPCE value of 29% at 420 nm. The order of the IPCE values for V-0.9 (19%), V-0.44 (15%), and V-0.3 (13%) at 420 nm is in line with the PEC results, proving that absorbing a high proportion of visible light remarkably enhances the PEC efficiency. For the evaluated bandgap from the IPCE values in Fig. 8d, the V-0.3 and V-0.44 samples showed bandgap values of 2.60 and 2.57 eV, and the V-0.3 and V-0.9 samples showed the same bandgap value of 2.53 eV. Nevertheless, V-0.9 showed a lower PEC performance than V-0.3 due to low IPCE efficiency in the range of 350 to 450 nm.

## 4. Conclusions

In summary, this study addressed the formation of heterostructured  $\text{BiVO}_4$  and  $\text{WO}_3$  with a mixed structure of NPs and linked  $\text{BiVO}_4$  NPs on  $\text{WO}_3$  nanocoral structures to enhance PEC performance. The linked  $\text{BiVO}_4$  NPs were simply constructed on anodic  $\text{WO}_3$  nanocorals by controlling the amount of the  $\text{BiVO}_4$  precursor to be 10  $\mu\text{L}$  during spin-coating. This phenomenon was related to the hydrophilicity of the  $\text{WO}_3$  nanocorals, as the precursor amount on the  $\text{WO}_3$  nanocorals that could withstand a high speed rpm during spin-coating was important. Furthermore, the linked  $\text{BiVO}_4$  NPs/ $\text{WO}_3$  nanocoral heterostructure showed improved PEC performance, including photocurrent density, PEC  $\text{H}_2$  production, and IPCE, compared to the  $\text{BiVO}_4$  NPs/ $\text{WO}_3$  nanocoral heterostructure. The linked NPs on the  $\text{WO}_3$  nanocorals provided photogenerated electrons to move to the  $\text{WO}_3$  substrate and improved the charge carrier and charge separation *via* the antenna effect. Moreover, the NPs did not

fully cover the  $\text{WO}_3$  nanocorals, and the nanocoral structures could harvest more light, which allowed for multiple light scattering. The optimized  $\text{BiVO}_4$  precursor concentration was 0.3 M of V and Bi, which formed the purest  $\text{BiVO}_4$  on the  $\text{WO}_3$  nanocorals without any by-product. When the V concentration was lower or higher than the Bi concentration,  $\text{Bi}_2\text{O}_3$  or  $\text{VO}_2$  was formed along with  $\text{BiVO}_4$ . Thus, the BW photoanode of the purist V-0.3 allowed realization of the highest photocurrent density and IPCE values of 0.45  $\text{mA cm}^{-2}$  (at 1.23 V vs. RHE) and 29% (at 420 nm), respectively, and accordingly the lowest charge transfer resistance of 486.9  $\Omega$ .

## Conflicts of interest

There are no conflicts to declare.

## Acknowledgements

This work was supported by Inha University Research Grant.

## References

- 1 Y. Park, K. J. McDonald and K.-S. Choi, *Chem. Soc. Rev.*, 2013, **42**, 2321–2337.
- 2 J. Lee, M. Kim, Y.-T. Kim and J. Choi, *Catal. Today*, 2022, **403**, 67–73.
- 3 K. Min, M. Kim, S. Min, H. Kim and S.-H. Baeck, *Appl. Surf. Sci.*, 2023, **624**, 157117.
- 4 M. Tayebi and B.-K. Lee, *Renewable Sustainable Energy Rev.*, 2019, **111**, 332–343.
- 5 V. S. Kumbhar, H. Lee, J. Lee and K. Lee, *J. Colloid Interface Sci.*, 2019, **557**, 478–487.
- 6 T. Kim, S. S. Patil and K. Lee, *Electrochim. Acta*, 2022, **432**, 141213.
- 7 B. Jin, E. Jung, M. Ma, S. Kim, K. Zhang, J. I. Kim, Y. Son and J. H. Park, *J. Mater. Chem. A*, 2018, **6**, 2585–2592.
- 8 F. F. Abdi, L. Han, A. H. Smets, M. Zeman, B. Dam and R. van de Krol, *Nat. Commun.*, 2013, **4**, 2195.
- 9 J. A. Seabold and K.-S. Choi, *J. Am. Chem. Soc.*, 2012, **134**, 2186–2192.
- 10 Y. Zhou, L. Zhang, L. Lin, B. R. Wygant, Y. Liu, Y. Zhu, Y. Zheng, C. B. Mullins, Y. Zhao, X. Zhang and G. Yu, *Nano Lett.*, 2017, **17**, 8012–8017.
- 11 X. Yao, D. Wang, X. Zhao, S. Ma, P. S. Bassi, G. Yang, W. Chen, Z. Chen and T. Sritharan, *Energy Technol.*, 2018, **6**, 100–109.
- 12 P. Lianos, *Appl. Catal., B*, 2017, **210**, 235–254.
- 13 Y. Pihosh, I. Turkevych, K. Mawatari, T. Asai, T. Hisatomi, J. Uemura, M. Tosa, K. Shimamura, J. Kubota, K. Domen and T. Kitamori, *Small*, 2014, **10**, 3692–3699.
- 14 S. S. Patil, J. Lee, E. Park, L. R. Nagappagari and K. Lee, *ACS Appl. Energy Mater.*, 2021, **4**, 13636–13645.
- 15 K. Fuku and K. Sayama, *Chem. Commun.*, 2016, **52**, 5406–5409.
- 16 J. Wang, T. Zhou, Y. Zhang, L. Li, C. Zhou, J. Bai, J. Li, H. Zhu and B. Zhou, *ACS Appl. Mater. Interfaces*, 2022, **14**, 45392–45402.





- 17 E. Park, S. S. Patil, H. Lee, V. S. Kumbhar and K. Lee, *Nanoscale*, 2021, **13**, 16932–16941.
- 18 B.-R. Huang, T.-C. Lin and Y.-M. Liu, *Sol. Energy Mater. Sol. Cells*, 2015, **133**, 32–38.
- 19 G. Zheng, J. Wang, H. Liu, V. Murugadoss, G. Zu, H. Che, C. Lai, H. Li, T. Ding, Q. Gao and Z. Guo, *Nanoscale*, 2019, **11**, 18968–18994.
- 20 J. Su, L. Guo, N. Bao and C. A. Grimes, *Nano Lett.*, 2011, **11**, 1928–1933.
- 21 A. A. M. Ibrahim, I. Khan, N. Iqbal and A. Qurashi, *Int. J. Hydrogen Energy*, 2017, **42**, 3423–3430.
- 22 Q. Pan, H. Zhang, Y. Yang and C. Cheng, *Small*, 2019, **15**, 1900924.
- 23 P. Chatchai, S. Kishioka, Y. Murakami, A. Y. Nosaka and Y. Nosaka, *Electrochim. Acta*, 2010, **55**, 592–596.
- 24 E. Park, T. Kim, J. Yoo and K. Lee, *Inorg. Chim. Acta*, 2023, **554**, 121538.
- 25 L. Xia, J. Bai, J. Li, Q. Zeng, X. Li and B. Zhou, *Appl. Catal., B*, 2016, **183**, 224–230.
- 26 J. Lee, S.-Y. Jung, V. S. Kumbhar, S. Uhm, H.-J. Kim and K. Lee, *Catal. Today*, 2021, **359**, 50–56.
- 27 L. Zhang, H. Zhang, B. Wang, X. Huang, Y. Ye, R. Lei, W. Feng and P. Liu, *Appl. Catal., B*, 2019, **244**, 529–535.
- 28 M. Saleem, M. F. Al-Kuhaili, S. M. A. Durrani, A. H. Y. Hendi, I. A. Bakhtiari and S. Ali, *Int. J. Hydrogen Energy*, 2015, **40**, 12343–12351.
- 29 N. Ghazkoob, M. Zargar Shoushtari, I. Kazeminezhad and S. M. Lari Baghal, *J. Alloys Compd.*, 2022, **900**, 163467.
- 30 T. G. U. Ghobadi, A. Ghobadi, M. C. Soydan, M. B. Vishlaghi, S. Kaya, F. Karadas and E. Ozbay, *ChemSusChem*, 2020, **13**, 2577–2588.
- 31 C.-y. Wang, C. Böttcher, D. W. Bahnemann and J. K. Dohrmann, *J. Mater. Chem.*, 2003, **13**, 2322–2329.
- 32 G.-C. Fan, H. Zhu, Q. Shen, L. Han, M. Zhao, J.-R. Zhang and J.-J. Zhu, *Chem. Commun.*, 2015, **51**, 7023–7026.
- 33 Y. Yan, R. W. Crisp, J. Gu, B. D. Chernomordik, G. F. Pach, A. R. Marshall, J. A. Turner and M. C. Beard, *Nat. Energy*, 2017, **2**, 17052.
- 34 L. Zhao, L. Miao, C. Liu, C. Li, T. Asaka, Y. Kang, Y. Iwamoto, S. Tanemura, H. Gu and H. Su, *Sci. Rep.*, 2014, **4**, 7000.
- 35 S. Wang, P. Chen, Y. Bai, J.-H. Yun, G. Liu and L. Wang, *Adv. Mater.*, 2018, **30**, 1800486.
- 36 F. Can, X. Courtois and D. Duprez, *Catalysts*, 2021, **11**, 703.
- 37 M. G. Yañez-Cruz, M. Villanueva-Ibáñez, F. Méndez-Arriaga, C. A. Lucho-Constantino, M. d. I. Á. Hernández-Pérez, M. d. R. Ramírez-Vargas and M. A. Flores-González, *J. Anal. Sci. Technol.*, 2022, **13**, 52.
- 38 I. Derkaoui, M. Khenfouch, I. Boukhoubza, M. Achehboune, R. Hatel, B. M. Mothudi, I. Zorkani, A. Jorio and M. Maaza, *Appl. Phys. A*, 2021, **127**, 934.
- 39 M. Wan, M. Xiong, S. Tian, X. Chen, B. Li, X. Lu and X. Zhao, *Materials*, 2023, **16**, 208.
- 40 M. R. d. S. Pelissari, N. F. Azevedo Neto, L. P. Camargo and L. H. Dall'Antonia, *Electrocatalysis*, 2021, **12**, 211–224.

